Supporting Information:

Modification of a buried interface with bulky organic cations for highly stable flexible perovskite solar cells

*Shyantan Dasgupta[a,b], Wiktor Żuraw[a,c], Taimoor Ahmad[d], Luigi Angelo Castriotta[e], Eros Radicchi[f,g], Wojciech Mróz[h,i], Mateusz Scigaj[d], Łukasz Pawlaczyk[j], Magdalena Tamulewicz-Szwajkowska[j], Marek Trzcinski[k], Jarosław Serafińczuk[j,l], Edoardo Mosconi[f], Aldo Di Carlo[e,m], Filippo De Angelis[f, n ,o], Alina Dudkowiak[b], Konrad Wojciechowski[a, d]**

*Corresponding author, konrad.wojciechowski@sauletech.com

[a] Saule Research Institute, Dunska 11, 54-427 Wroclaw, Poland

[b] Faculty of Materials Engineering and Technical Physics, Poznan University of Technology, Piotrowo 3, 60-965 Poznan, Poland

[c] Department of Semiconductor Materials Engineering, Wroclaw University of Science and Technology, Wybrzeze Wyspianskiego 27, 50-370, Wroclaw, Poland

[d] Saule Technologies, Dunska 11, 54-427 Wroclaw, Poland

[e] Centre for Hybrid and Organic Solar Energy (CHOSE), Department of Electronic Engineering, University of Rome Tor Vergata, Rome, 00133, Italy

[f] Computational Laboratory for Hybrid/Organic Photovoltaics (CLHYO), Istituto CNR di Scienze e Tecnologie Chimiche "Giulio Natta" (CNR-SCITEC), via Elce di Sotto 8, Perugia (PG), I-06123 Italy.

[g] Nanomaterials Research Group, Department of Biotechnology, University of Verona, Strada Le Grazie 15, I-37134 Verona, Italy.
[h] Centre for Nano Science and Technology (CNST@PoliMi), Istituto Italiano di Tecnologia (IIT), Via Pascoli, 70/3, 20133, Milano, Italy
[i] Istituto di Scienze e Tecnologie Chimiche "Giulio Natta" (SCITEC),Consiglio Nazionale delle Ricerche, v. A. Corti 12, 20133 Milan, Italy
[j] Department of Nanometrology, Wroclaw University of Science and Technology, Janiszewskiego 11/17, 50-372 Wroclaw, Poland
[k] Institute of Mathematics and Physics, Bydgoszcz University of Science and Technology; Al. S. Kaliskiego 7; 85-796 Bydgoszcz
[l] Łukasiewicz Research Network – PORT Polish Centre for Technology Development, Stablowicka 147, 54-066 Wroclaw, Poland
[m] Istituto di Struttura della Materia (ISM-CNR), Via del Fosso del Cavaliere 100, Rome, 00133, Italy
[n] Dipartimento di Chimica, Biologia e Biotecnologie, Università degli Studi di Perugia & UdR INSTM di Perugia, via Elce di Sotto 8, 06123, Perugia, Italy.
[o] Department of Natural Sciences & Mathematics, College of Sciences & Human Studies, Prince Mohammad Bin Fahd University, Al Khobar 31952, Saudi Arabia.

I. EXPERIMENTAL SECTION

a) Materials

Unless otherwise stated, all the materials were purchased from Sigma-Aldrich and used as received. Indium-doped tin oxide (IZO)-coated polyethylene terephthalate (PET) substrates (sheet resistance of 15 $\Omega\ \square^{-1}$) were bought from Eastman Chemical Company, phenethylammonium iodide (PEAI) and 4-fluoro-phenethylammonium iodide (FPEAI) were purchased from Greatcell Solar, formamidinium iodide (FAI) was purchased from Ajay North America, poly[bis-(4-phenyl)

(2.4.6-trimethylphenyl) amine (PTAA) was pucharsed from Ossila. Silver (Ag, 99.99%), gold (Au, 98.99%), and copper (Cu, 99.99%) were purchased from Kurt. J. Lesker. Perovskite precursor solutions (nominal perovskite composition: $Cs_{0.17}FA_{0.83}Pb(I_{0.9}Br_{0.1})_3$ were prepared with a concentration of 1.45 M, following the recipe: 64 mg of cesium iodide (CsI, 98%), 79.8 mg of lead bromide ($PbBr_2$, 98%), 207 mg of FAI, and 568.2 mg of lead iodide (PbI_2, 99.999%) were dissolved in 1 mL of a 4:1 N,N-dimethylformamide (DMF)/dimethyl sulfoxide (DMSO) volume ratio. 18C6, a crown ether-based additive was added to the solution at a concentration of ≈ 0.2 mg mL^{-1}.

b) Processing

Device fabrication

Flexible PSCs were fabricated with the following architecture: PET/IZO/PTAA/$Cs_{0.17}FA_{0.83}Pb(I_{0.9}Br_{0.1})_3$/$C_{60}$/BCP/Ag. PET/IZO substrates (18 × 13 mm^2 pieces) were patterned by dipping one side in the HCl solution (15 wt% in deionized (DI) water). The etched substrates were cleaned by ultrasonication in DI water and isopropanol for 7 minutes in each solvent and dried by nitrogen flow. Before layer processing, substrates were treated with oxygen plasma for 30 seconds. PTAA solution (2 mg mL^{-1} in toluene) was spin coated under ambient conditions at 5000 rpm for 30 seconds, followed by annealing at 100 ℃ for 10 minutes, which resulted in a ~20 nm thick film. After this process, the samples were transferred into a nitrogen-filled glovebox. FPEAI and PEAI solutions were prepared by dissolving the respective powders in a concentration of 5 mg mL^{-1} in DMF and spin coated at 4000 rpm for 30 seconds and annealed for 5 minutes at 100˚C. Perovskite solution was spin coated onto the substrates at 6000 rpm for 30 seconds with a ramping rate of 2000 rpm s^{-1}. 150 µL of anhydrous ethyl acetate was

dripped as an antisolvent on the substrate at the 7th second after the spinning sequence commenced. The perovskite layer was first dried for 2 minutes, then pre-heated at 50˚C for 10 minutes and finally annealed at 100 ˚C for 1 hour. The electron transporting layer of fullerene C_{60} (30 nm) was deposited using thermal evaporation. Finally, 6 nm of bathocuproine (BCP) buffer layer and 95 nm of Ag electrode were deposited on top of devices by thermal evaporation at ~10^{-6} mbar.

Lift-Off process

This process was similar to a process reported by Zhu et al.[1] A PTAA solution of 40 mg mL^{-1} in toluene was spin coated on the pre-cleaned PET/IZO substrates and annealed at 100°C for 10 minutes in an ambient atmosphere. The PTAA layer acted as a sacrificial layer for the lift-off process. The perovskite layers, with and without the BOC molecules, were deposited in an aforementioned manner. The samples were then coated with the 200 nm of Cu electrode layer, done by thermal evaporation. The samples were then immersed in a chlorobenzene solution, where PTAA was solubilized. The free-floating perovskite films, with and without the BOC passivation, were subsequently placed on fresh substrates, cleaned twice with anhydrous chlorobenzene and used for characterization measurements.

c) Characterization methods

Current-voltage measurements

Stabilized power output and J-V measurements were carried out by a Keithley 2461 source measure unit (SMU). The solar cells were illuminated with a simulated AM1.5G irradiation of 100 mW/cm^2 using an AAA-rated solar simulator obtained from Abet Technologies, sun 2000 which was calibrated against an RR-208-KG5 silicon reference cell also procured from Abet Technologies. Solar cells were masked with a 0.616 cm^2 shadow mask. JV measurements were carried out in two different scan directions namely reverse scan and forward scan i.e., from forward bias to short-circuit, and from short-circuit to forward bias respectively. The scanning rate was set to 500 $mV{\cdot}s^{-1}$. The Stabilised power output measurement was carried out at the maximum power point voltage for 30 seconds.

External Quantum Efficiency

The EQE spectra was obtained by using the Bentham PVE300 photovoltaic characterization system with the help of an installed control software BenWin+.

Photoluminescence measurements

Steady-state photoluminescence (ss-PL) and time-resolved photoluminescence (TRPL) measurements were performed with the Edinburgh Instruments FS5 Spectrofluorometer, which was equipped with a time correlated single photon counting (TCSPC) unit. Samples were excited with a 405 nm laser diode (60 ps pulse, intensity: 15 mW/cm^2).

Electroluminescence measurements

Electroluminescence (EL) spectra of the solar cells were recorded using an Ocean Optics Maya 2000 Pro spectrometer. Voltage was applied to the devices with a Keithley 2614B source meter, either by performing voltage scans or by applying constant bias. The emitted light was detected by a calibrated photodiode which was in contact with the cells. This characterization was performed in ambient conditions without any encapsulation route.

Scanning electron microscopy

Cross-section images were developed by deploying a focus ion beam scanning electron microscope, FIB-SEM (FEI Helios 600), which had an accelerating voltage of 2 kV. The samples for measurement were prepared by depositing a carbon and platinum films on the top side. Top-view morphology images of samples were obtained with a field emission SEM (Phenom ProX), which had an accelerating voltage of 5 kV with a working distance of 8.0 mm.

X-ray diffraction measurements

X-ray diffraction (XRD) patterns were collected with two different X-ray diffractometers: Rigaku MiniFlex600 (Cu Kα radiation, λ=1.5406 Å), and MRD-Philips's diffractometer supported by the parallel beam optic with 0.1 mm slit in the diffracted beam path (Cu Kα radiation, λ=1.540597 Å). Using the above configuration, respective samples were measured using theta-2theta scans.

AFM measurements

The AFM measurements were carried out with a Veeco/Bruker Nanoman V microscope.

c-AFM measurements

For the c-AFM measurements, the temperature was fixed at 19.5-20°C. Humidity was controlled at 30%. Samples were grounded using electrically conductive silver paint (Silver Conductive Adhesive 503, Electron Microscopy Sciences). Measurements were performed in dark (no light) and bright mode (AFM internal halogen light set to 100%). The samples were kept in the dark for

1 hour before the start of the measurements. An Arrow Cont-Pt cantilever was used (force constant of 0.36 N/m). A constant contact force of 10 nN was applied to the sample during the measurements. The samples were biased at 0, 0.5V, and -0.5V.

X-ray Photoelectron Spectroscopy measurements

The XPS (X-ray Photoelectron Spectroscopy) measurements were performed under UHV (Ultra-high vacuum) conditions. Base pressure in the analysis chamber was $\leq 2 \cdot 10^{-10}$ mbar. The photoemission process was initiated using an AlKα radiation source (1486.6 eV) oriented at 55° to the normal of the samples. The energy of the photoelectrons was determined with the VG-Scienta R3000 spectrometer. The energy step was set to $\Delta E = 0.1$ eV. Experimental data were then fitted to Gauss-Lorentz shapes with Shirley background using CasaXPS® software. The atomic concentrations of the surface components of the samples were determined by fitting the experimental data to Gauss-Lorenz shapes and taking into account the relative sensitivity factors (RSF). CasaXPS software was used for this purpose.

II. ADDITIONAL DATA

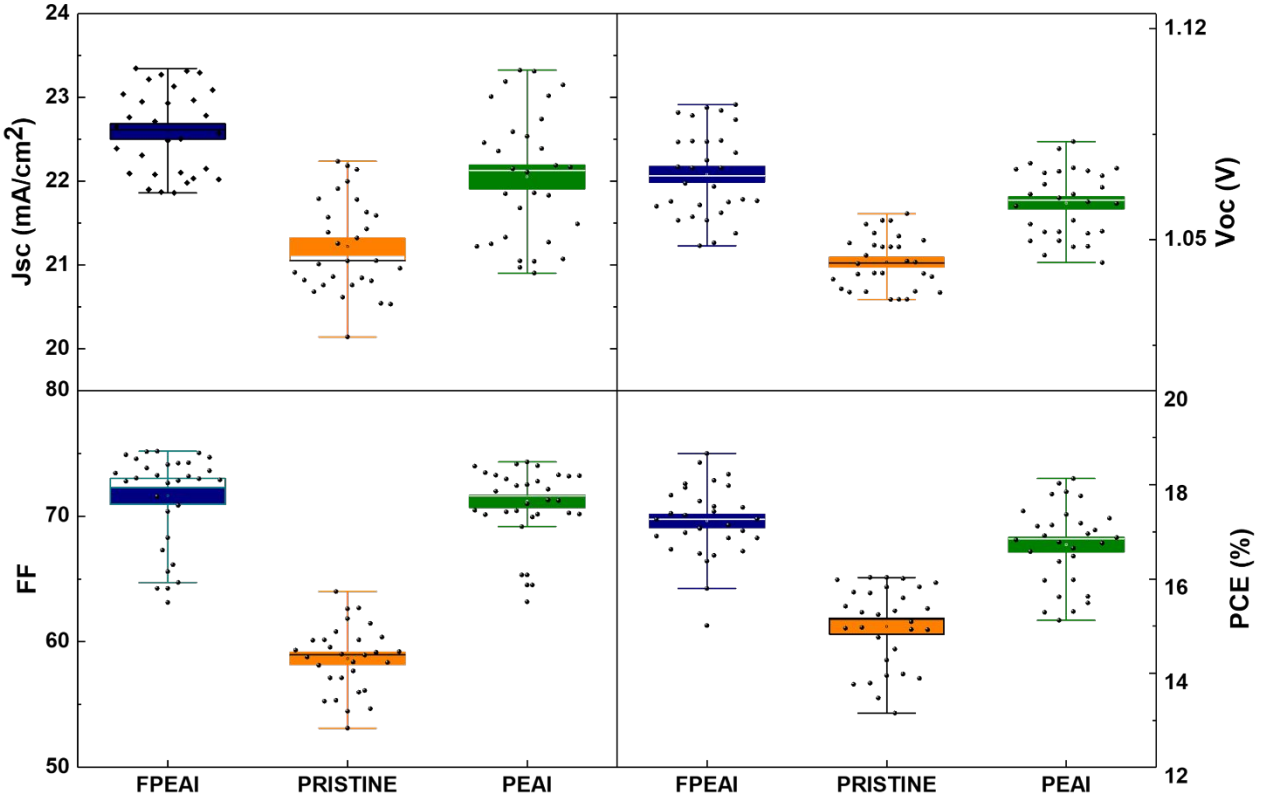

Figure S1. Statistics of photovoltaic performance parameters extracted from the J-V characteristics of perovskite solar cells, with and without interface modification.

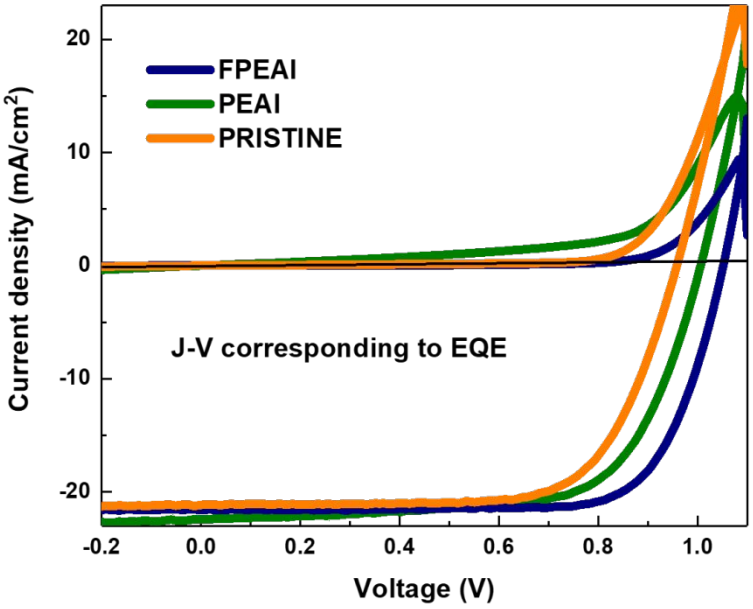

Figure S2. J-V curves (reverse scans) of perovskite solar cells for which EQE spectra were displayed in **Figure 1e**.

Table S1. Photovoltaic parameters extracted from the current-voltage characterization measurements of the perovskite solar cells fabricated with and without interface modification layers corresponding to **Figure S2**.

Sample (EQE)	PCE (%)	J_{SC} (mA/cm^2) from EQE	FF (%)	V_{OC} (V)
PEAI	15.19	21.20	67.51	1.00
FPEAI	16.95	21.40	75.03	1.04
PRISTINE	14.15	21.02	70.28	0.95

Supplementary Note 1

Density Functional Theory (DFT) calculations have been carried out on the (001) $FAPbI_3$ surface within the supercell approach at the gamma point of the Brillouin zone, by using the Perdew-Burke-Ernzerhof (PBE) functional[2], ultrasoft pseudopotentials (shells explicitly included in calculations: I 5s, 5p; N, C, F 2s, 2p; H 1s; Pb 6s, 6p, 5d), a cut-off on the wavefunctions of 40 Ryd (320 Ryd on the charge density) and including DFT-D3 dispersion interaction.[3] All calculations were performed by using the Quantum Espresso package.[4] Slabs models have been built starting from the tetragonal phase of $FAPbI_3$, by fixing cell parameters to the experimental values.[5] More than 10 Å of vacuum were added along the non-periodic direction perpendicular to the slabs in all cases to make sure the replicas were not interacting along the corresponding axis. Asymmetric disposition of the organic cations on the external layers of the slabs has been adopted in all cases, leading to supercells with zero average dipole moments. Such arrangement of organic cations provided an almost flat electrostatic potential in the vacuum region of the supercells for all the modelled slabs. Figures of the simulated systems were constructed with the Mercury software.[6]

The cation and salt exchange energies, $E_{exc,\ cat}$ and $E_{exc,salt}$, were evaluated as per Equation S1 and S2, respectively:

$$E_{exc,cat} = E_{tot} + n * E_{FA+} - (E_{I-term} + n * E_{cation}) \quad \text{S1}$$

$$E_{exc,cat} = E_{tot} + n * E_{FAI} - (E_{I-term} + n * E_{salt}) \quad \text{S2}$$

where E_{tot} is the total energy of the substituted system; $E_{I\text{-}term}$ is the energy of the FAI-terminated slab; E_{FA+} / E_{FAI} is the energy of the FA^+ cation / FAI salt; E_{cation} / E_{salt} is the energy of the substituted cation / salt; n is the number of substitutions.

Table S2. Exchange energies of *n* units of FA^+ (FAI) with PEA^+(PEAI) or $FPEA^+$(FPEAI). Values in eV.

n	$E_{exc,cat}$		$E_{exc,salt}$	
	PEA^+	**$FPEA^+$**	**PEAI**	**FPEAI**
1	0.09	-0.03	0.07	0.03
2	-0.25	-0.41	-0.30	-0.30
3	-0.31	-0.56	-0.37	-0.40

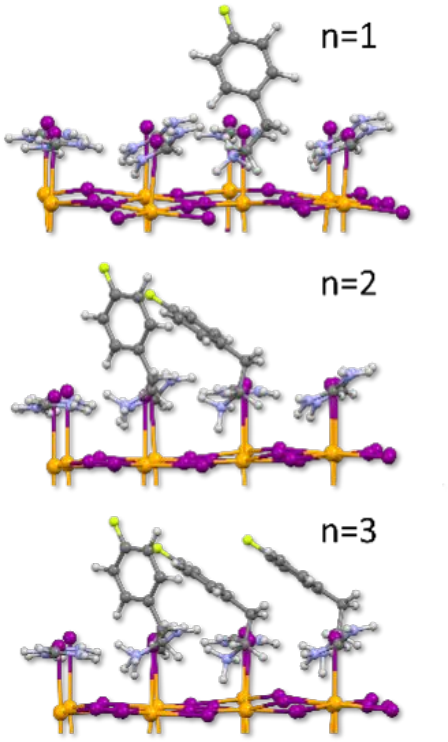

Figure S3. Exchange process of FA^+ with PEA^+/$FPEA^+$, for n = 1 to 3.

The projected densities of states (DOS) have been calculated at the PBE level and aligned to the vacuum level in all cases, see **Figure S4**.

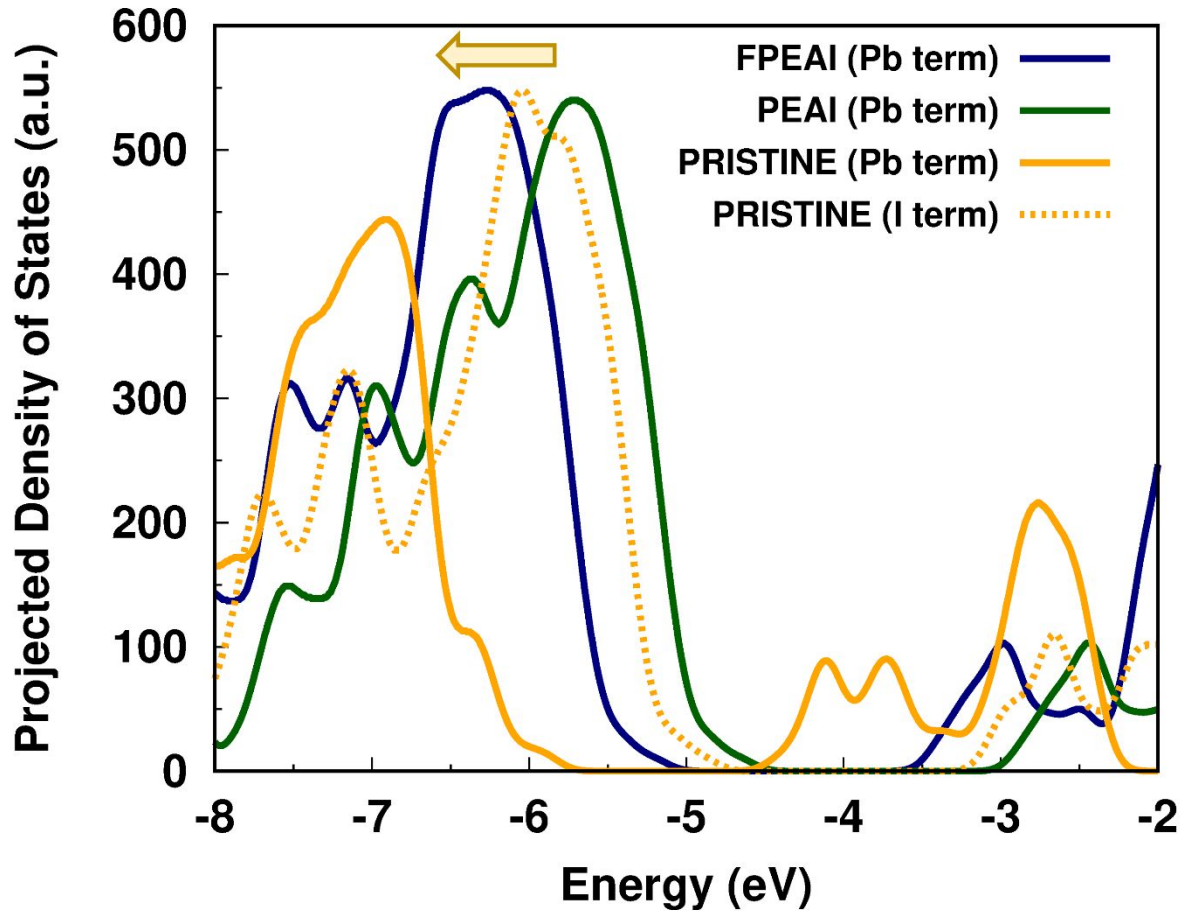

Figure S4. Projected density of states (DOS) of pristine and PEAI/FPEAI passivated systems. The arrow indicates the energy downshift from the PEAI- to FPEAI-passivated system.

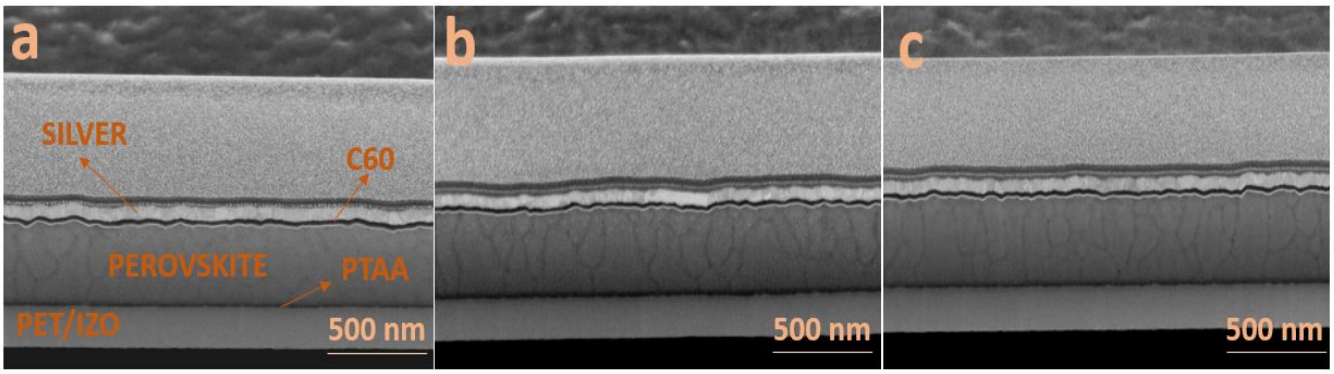

Figure S5. FIB-SEM cross-section image of the p-i-n configured perovskite solar cell of (a) pristine (b) PEAI and (c) FPEAI based modification.

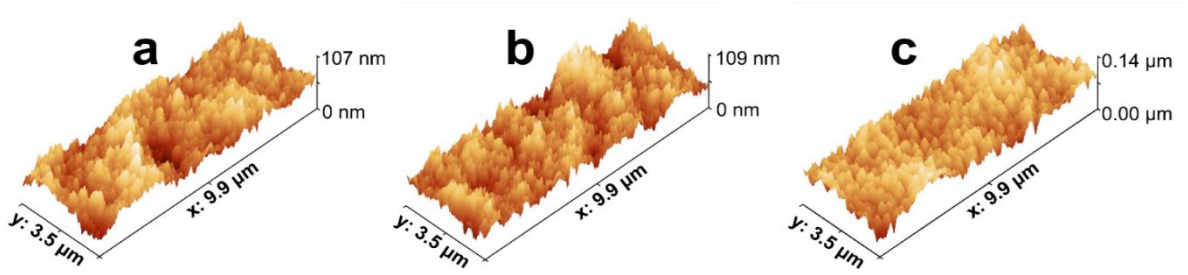

Figure S6. AFM 3D surface topography images (scanning range: 3.5 µm x 9.9 µm) of perovskite films, processed on (a) FPEAI-passivated PTAA, (b) PEAI-passivated PTAA, and (c) pristine PTAA layer.

Table S3. Surface roughness parameters extracted from the AFM imaging.

Sample	Roughness Average [nm]	RMS Roughness (Sq) [nm]	Mean Roughness (Sa) [nm]
FPEAI	56.7	12.9	10.0
PEAI	54.8	13.2	10.5
PRISTINE	82.0	14.9	11.7

Supplementary Note 2.

The method described by Zhao et al. and Dasgupta et al. was applied to obtain micro strain values.[7,8] The described method enables the determination of strain in nanocrystalline materials by examining the variability of the width of the reflections. The reflections (110), (220), (330) were taken for analysis. These reflections positions are: 14.2°, 28.6° and 43.5°. The (440) reflection due to its low intensity was not included in the analysis.[9,10] This method uses the assumption that the full width at half maximum (FWHM) of the diffraction peak is affected by several factors, including strain and the finite size of crystallites. In this particular case, the most important factors taken into account are apparatus expansion, grain size and strain as shown in the **Supporting Information Equation** 3 below

$$\Delta d_{obs}^2 = \Delta d_{ins}^2 + \Delta d_{size}^2 + \Delta d_{\varepsilon}^2 \qquad \text{S3}$$

Where:

Δd_{obs}^2 - full width at half maximum (FWHM) of the reflection,

Δd_{ins}^2 - instrument contribution - FWHM broadening of a selected reflection caused by the XRD apparatus,

Δd^2_{size} - grain size contribution,

Δd^2_{ε} – micro strain contribution.

We assume that the strain value $\varepsilon = \frac{\Delta d}{d}$ and that it is expressed on the universal scale of interplanar distance - d spacing: $d = \frac{\lambda}{2sin\theta}$. Thanks to this, we can write the **Supporting Information Equation 4** as:

$$\Delta d^2_{obs} - \Delta d^2_{ins} = \varepsilon^2 d^2 + \Delta d^2_{size} \quad \text{S4}$$

This equation can be compared to the line equation y = ax + b. As a result, the sought value of ε can be determined from the slope of the line drawn for reflections from the same families of crystallographic planes as shown in **Figures S7**a and b.

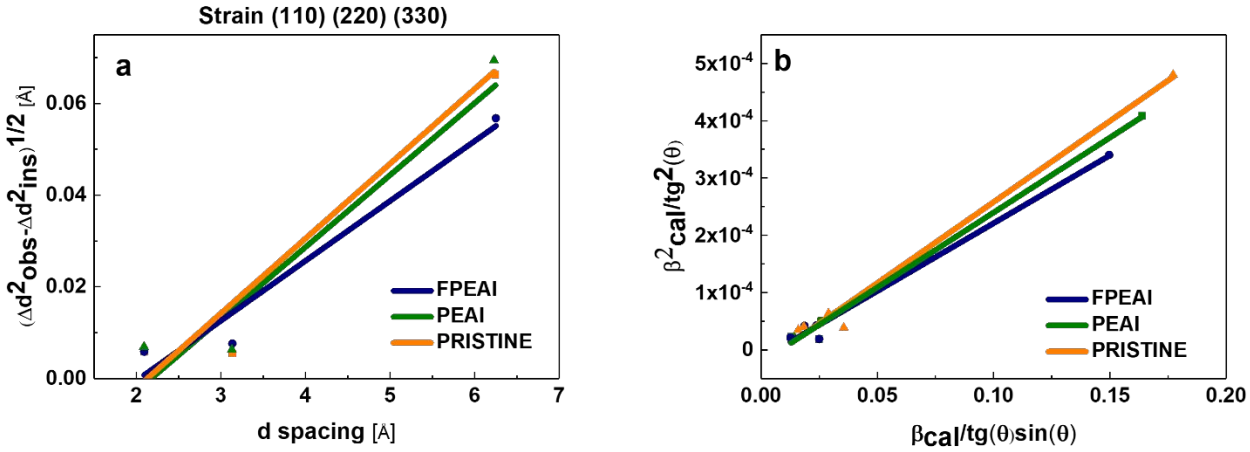

Figure S7. Williamson-Hall plot for Perovskite films with and without interface modification, (a) for micro strain determination: $(\Delta d^2_{obs} - d^2_{ins})^{1/2}$ *versus* d, according to equation (S4); (b) for crystallite size determination, based on reflections (110), (220) and (330), β is the FWHM value of the reflection.

To determine the average size of crystallites in the structure, the Williamson-Hall (W-H) method was used.[11] The following reflections were analyzed: (110), (112), (224), (312), (314). By drawing a plot of $\beta^2_{cal}/tg^2(\theta)$ vs. $\beta^2_{cal}/tg^2(\theta)\sin(\theta)$ it is possible to determine the size of the crystallites from the slope a, using the **Supporting Information Equation 5** below.

$$D = \frac{k\lambda}{a} \quad \text{S5}$$

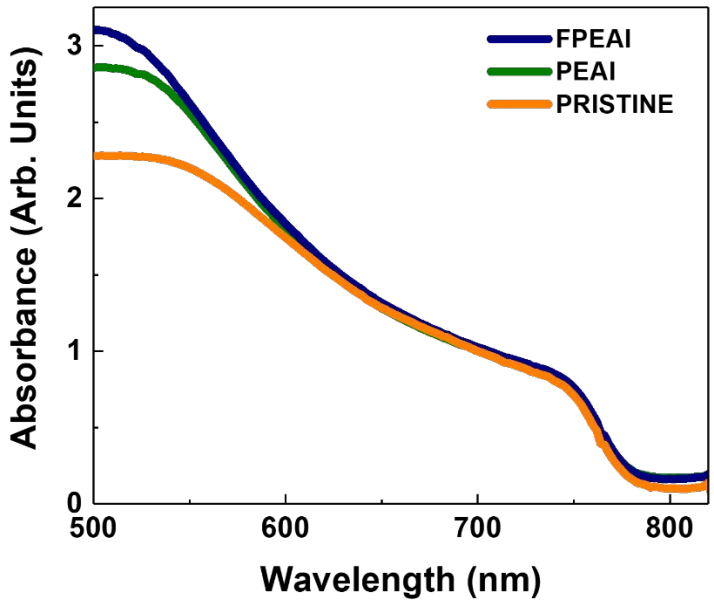

Figure S8. UV-Vis spectra of perovskite thin films processed on the three different surface variations.

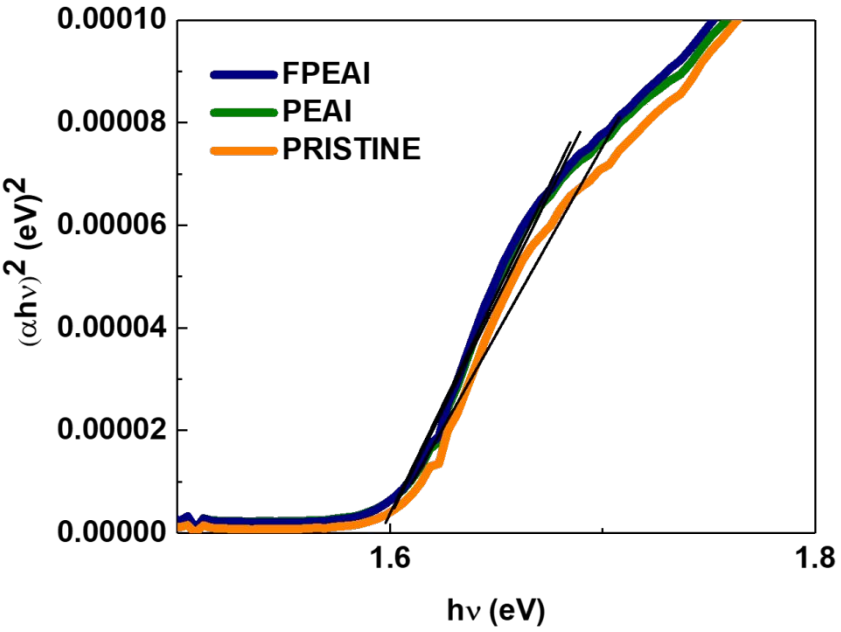

Figure S9. Tauc plots of perovskite layers processed on the studied surface variaitions.

Table S4. PL lifetimes derived from the decay curves with the non-linear exponential fits.

Sample	Lifetime (ns) with PTAA layer	Lifetime (ns) without PTAA layer/lift-off films
FPEAI	439.5	1135
PEAI	254.5	481
PRISTINE	148.8	208

Supplementary Note 3

To have more insight into the device operation principles, we applied the Shockley diode equation to the EL results following **Equation S6**:

$$I = I_s\left(e^{\frac{eU}{nkT}} - 1\right) \quad \text{S6}$$

where I is current in the diode, I_S stands for the saturation current, U denotes the voltage applied to the device, n is the ideality factor, and the other symbols have their previous meanings. In **Figure S11a-c**, we display the results for the best fits to the Shockley equation. The temperature was fixed to 320 K for the calculations. For lower voltages, the influence of shunt resistances is visible, while for higher applied biases, series resistance becomes more significant.[12] The values of the fitting parameters (the saturation currents and ideality factors) are reported in **Table 3** in the main text and in the **Figure S11**. In the studied sample types, the ideality factors and saturation currents display the following trend: pristine > PEAI > FPEAI, which means that the latter is the closest to the ideal diode.

Alternatively, **Equation S6** can be further transformed to **Equation S7**, which allows direct calculation of the ideality factor:

$$n = \left(\frac{kT\partial \ln I}{e\ \partial U}\right)^{-1} \quad \text{S7}$$

Application of this method instead of the best fit to **Equation S6** gives information about the validity of the fitting procedure.[13] **Figure S11d** presents the ideality factors calculated from **Equation S7**, applied to the currents from **Figure S11a-c**. The value of the ideality factor is indicated by the curve's minimum. The pristine sample data indicate that a single exponent is not sufficiently good to fit the current of this device, because the voltage range where its ideality factor is constant, is too narrow. The situation improves slightly for the PEAI-passivated samples, and for the FPEAI-passivated device the ideality factor does not change between 0.75 and 0.95 V, and therefore for this voltage range the fit is done with **Equation S6** works well. A comparison

between the ideality factors obtained from the two methods suggests that in the pristine device resistance is the highest and decreases with improvement of the PTAA/perovskite interface. For the FPEAI-modified cell the ideality factors are the closest to each other and approach 2, a value typically attributed to a first order (monomolecular) recombination process, e.g., with an assistance of traps localized within a band gap. However, as shown by many authors, such a simple explanation is often not correct since correlation between ideality factor and recombination processes is a more complex relation.[14,15] We can therefore give a tentative conclusion that an improvement of the solar cells' performance was caused by decrease of resistance at the PTAA/$CsFAPbI_3$ interface, but a nature of processes responsible for charge carrier recombination cannot be simply derived from the ideality factors.

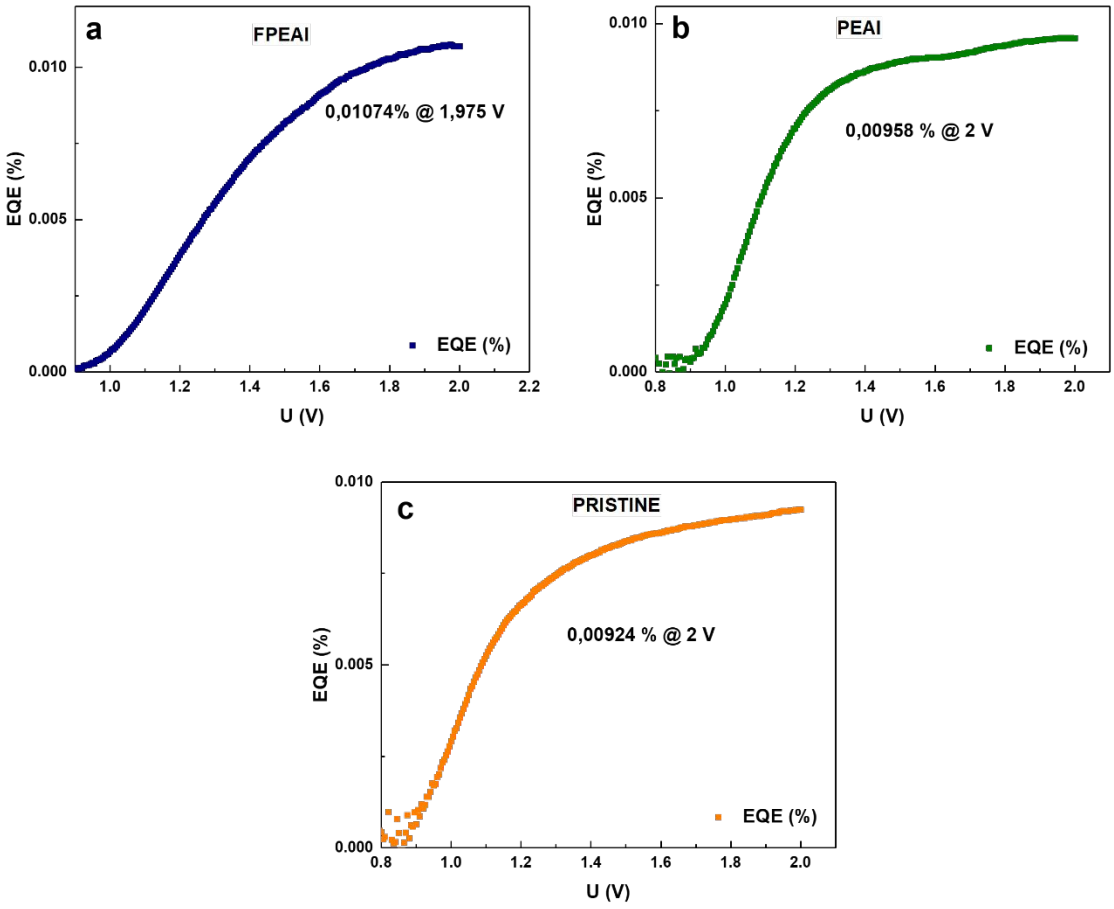

Figure S10. EL external quantum efficiencies as a function of applied voltage for the three types of devices: (a) FPEAI-passivated, (b) PEAI-passivated, and (c) pristine.

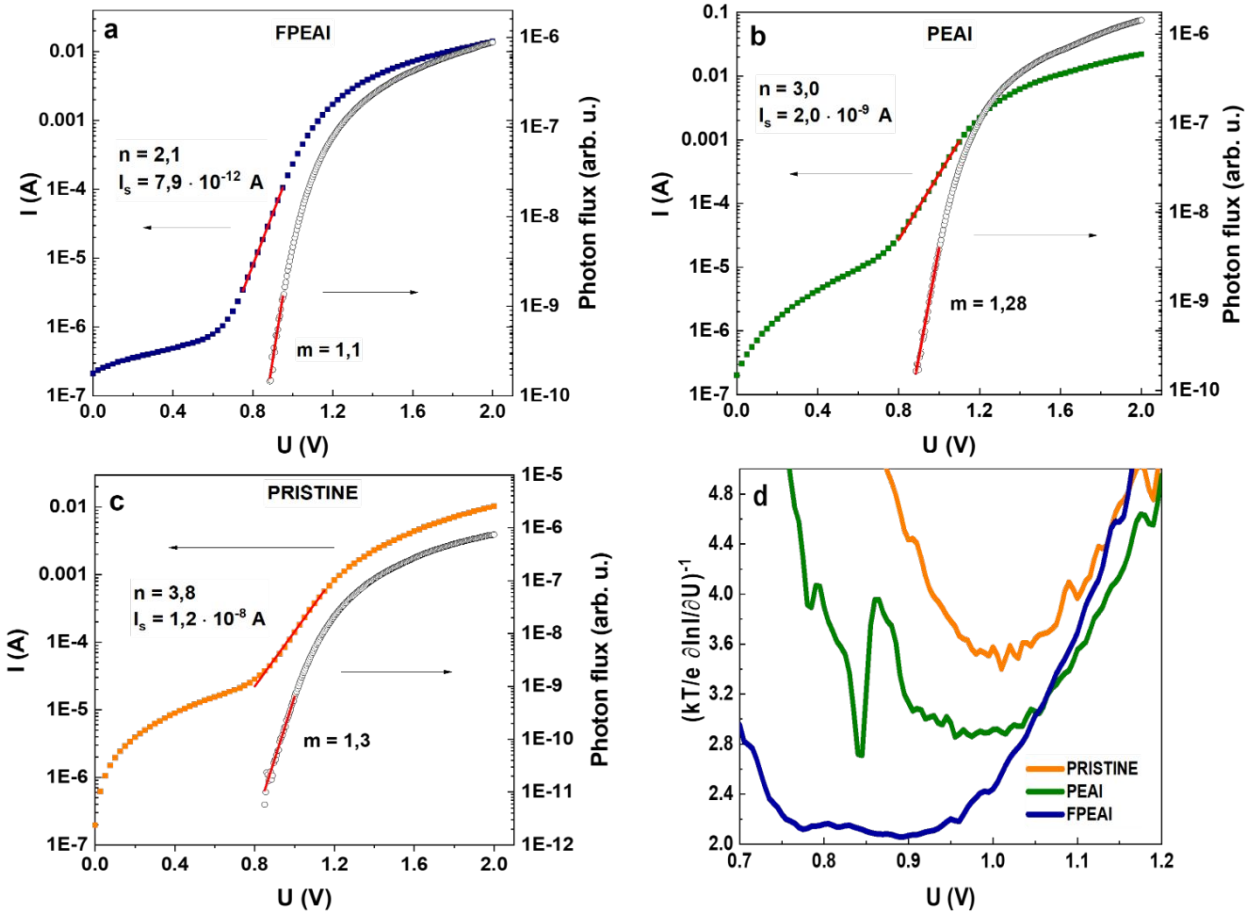

Figure S11. Currents and photon fluxes as a function of applied voltage for the three types of devices: (a) FPEAI-passivated, (b) PEAI-passivated, and (c) pristine. Saturation currents (I_s) and ideality factors for currents (n) and photon fluxes (m) are calculated from the best fits to Equation (S6). Temperature was fixed to 320 K. d) Ideality factors calculated from Equation S7 (for the currents shown in Figure **S**11a-c, with temperature fixed at 320 K).

Table S5. Average currents measured in the c-AFM measurement for the three sample types, under dark and light conditions at different biases corresponding to **Figure 5**f.

Sample Bias [V]	Measured current [pA]					
	FPEAI		PEAI		PRISTINE	
	DARK	BRIGHT	DARK	BRIGHT	DARK	BRIGHT
0	-55	-61.5	-29.8	-21.6	-10.5	-3.2
-0.5	-296	-255.6	-204.3	-123.0	-73.9	-37.7
+0.5	10.64	15.1	8.5	3.4	1.31	1.4

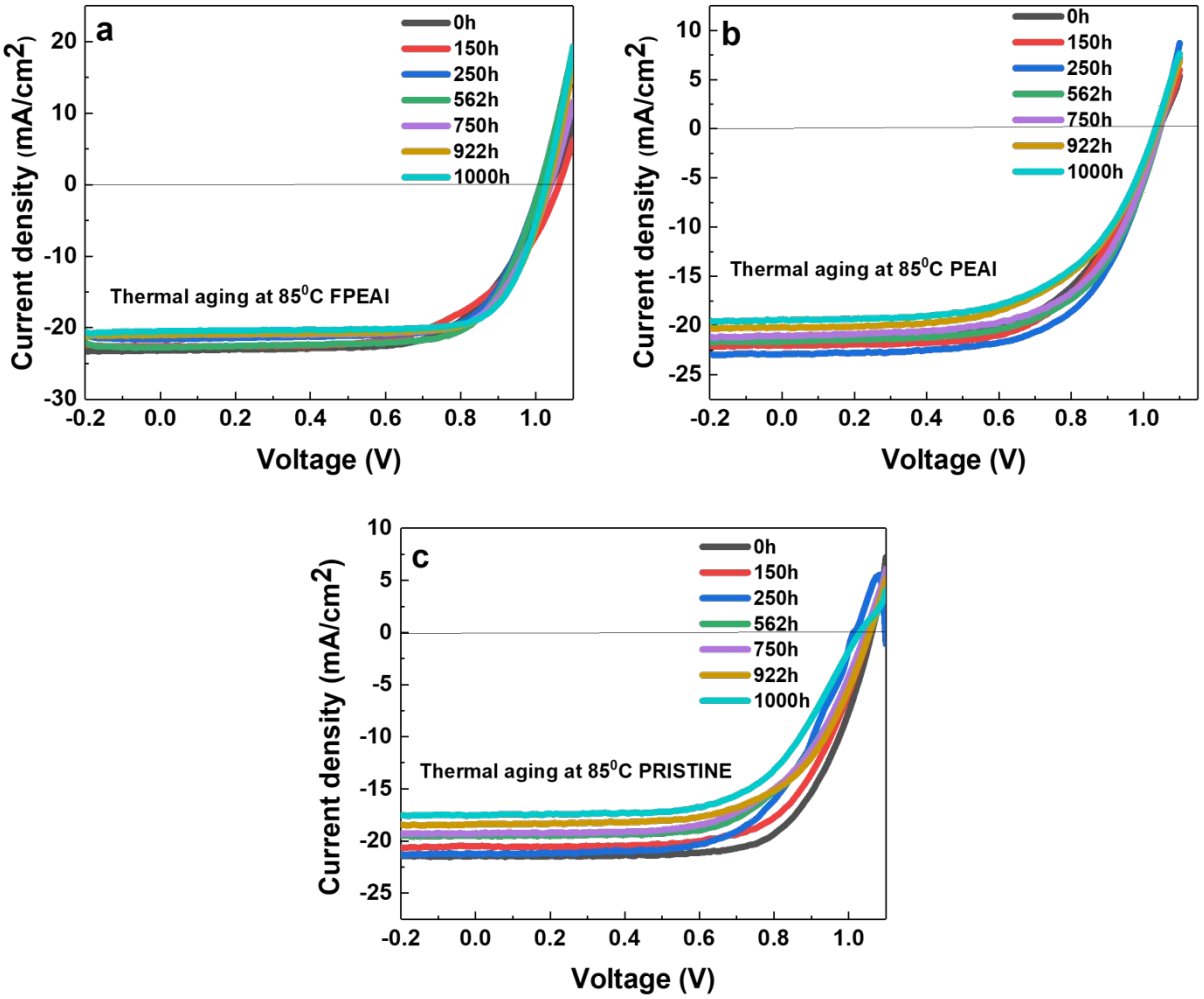

Figure S12. J-V curves (reverse scans) of the three types of devices: a) FPEAI-passivated, b) PEAI-passivated, and c) pristine, taken along the aging test at 85°C.

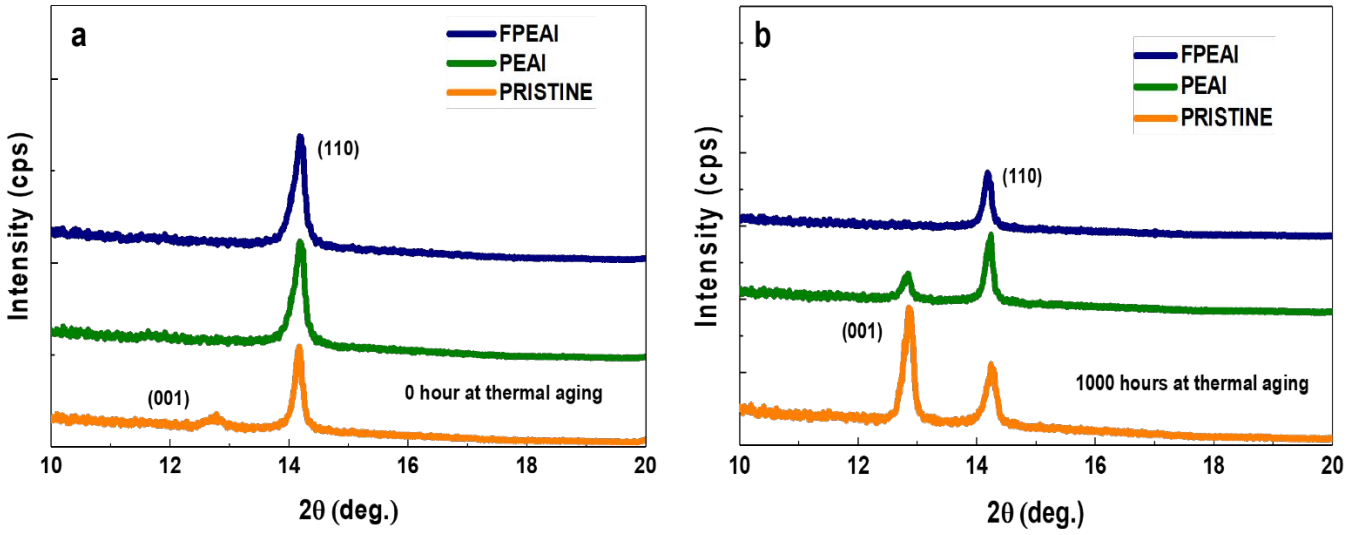

Figure S13. X-ray diffractograms of perovskite layers processed on the three different surface variations (FPEAI-, PEAI-modified, and pristine), taken (a) before aging, and (b) after 1000 hours of thermal test at 85°C.

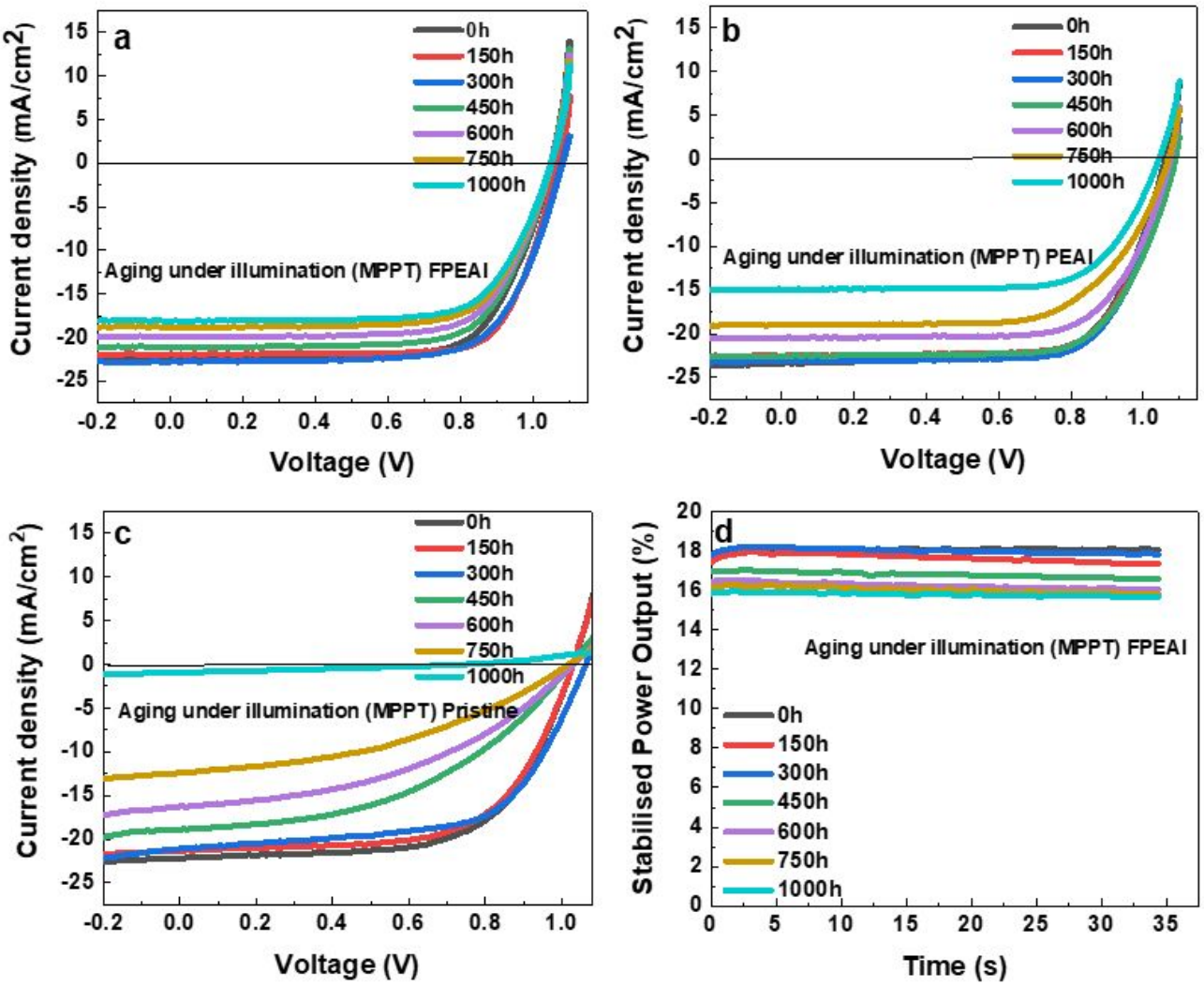
a
Current density (mA/cm2)
Voltage (V)
0h
150h
300h
450h
600h
750h
1000h
Aging under illumination (MPPT) FPEAI
b
Current density (mA/cm2)
Voltage (V)
0h
150h
300h
450h
600h
750h
1000h
Aging under illumination (MPPT) PEAI
c
Current density (mA/cm2)
Voltage (V)
0h
150h
300h
450h
600h
750h
1000h
Aging under illumination (MPPT) Pristine
d
Stabilised Power Output (%)
Time (s)
Aging under illumination (MPPT) FPEAI
0h
150h
300h
450h
600h
750h
1000h

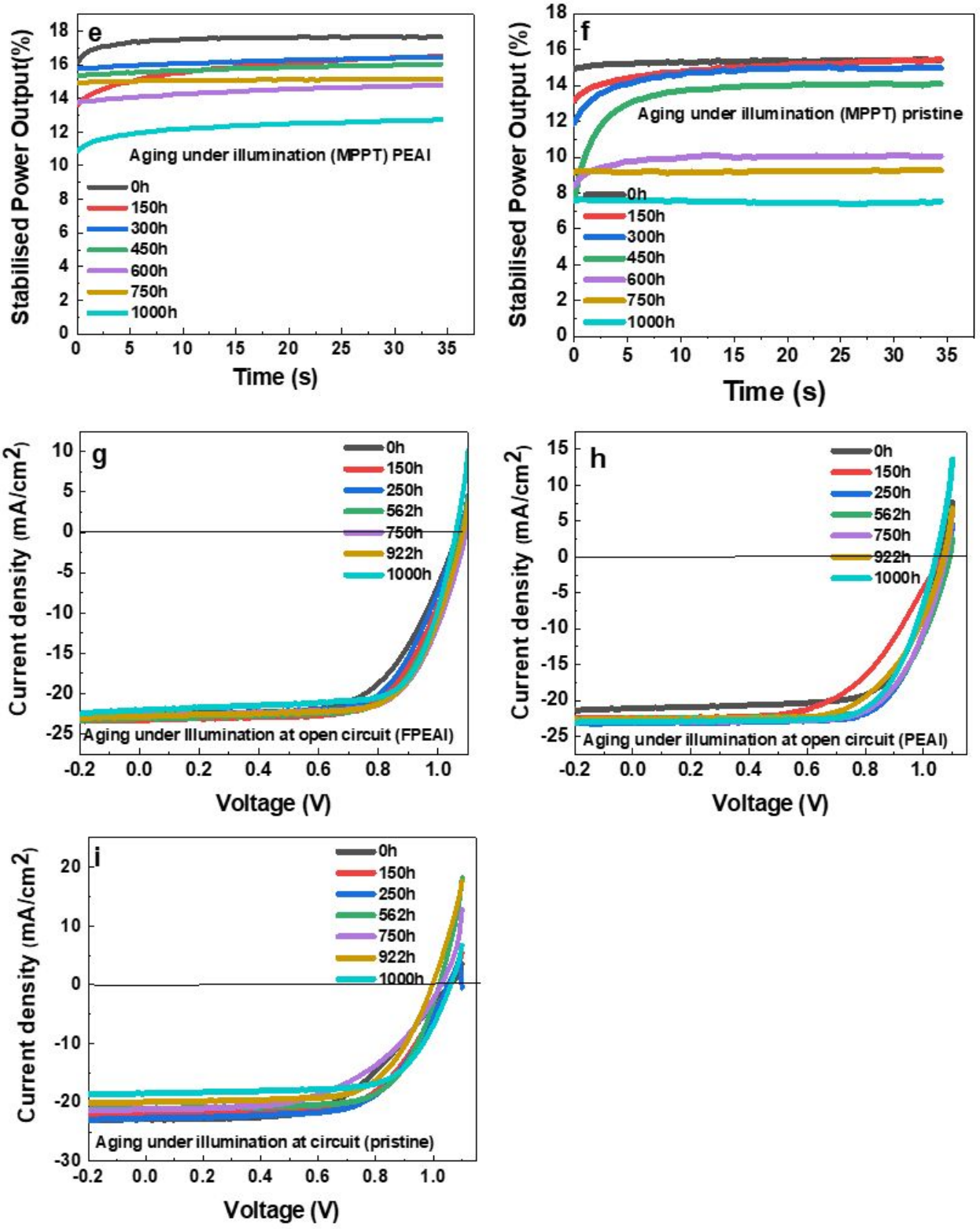

Figure S14. J-V curves (reverse scans) of the three types of devices: (a, g) FPEAI-passivated, (b, h) PEAI-passivated, and (c, i) pristine, taken along the operational aging test at MPP (a-c) and light soaking at V_{OC} (h-i).; (d-f) SPO curves of the same device variations, aged at MPP.

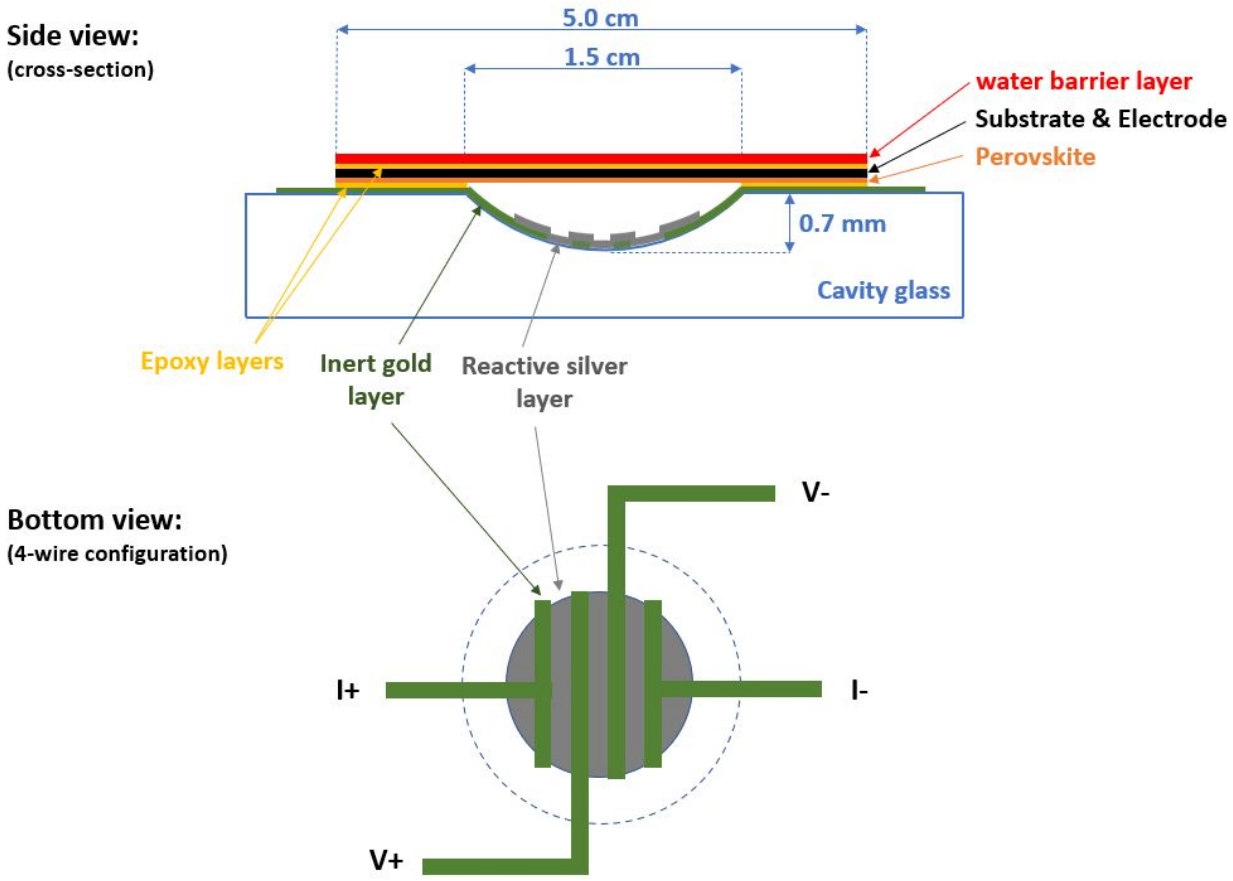

Figure S15. Schematic of the sample setup for the iodine release monitoring, which is based on silver conductance measurement.

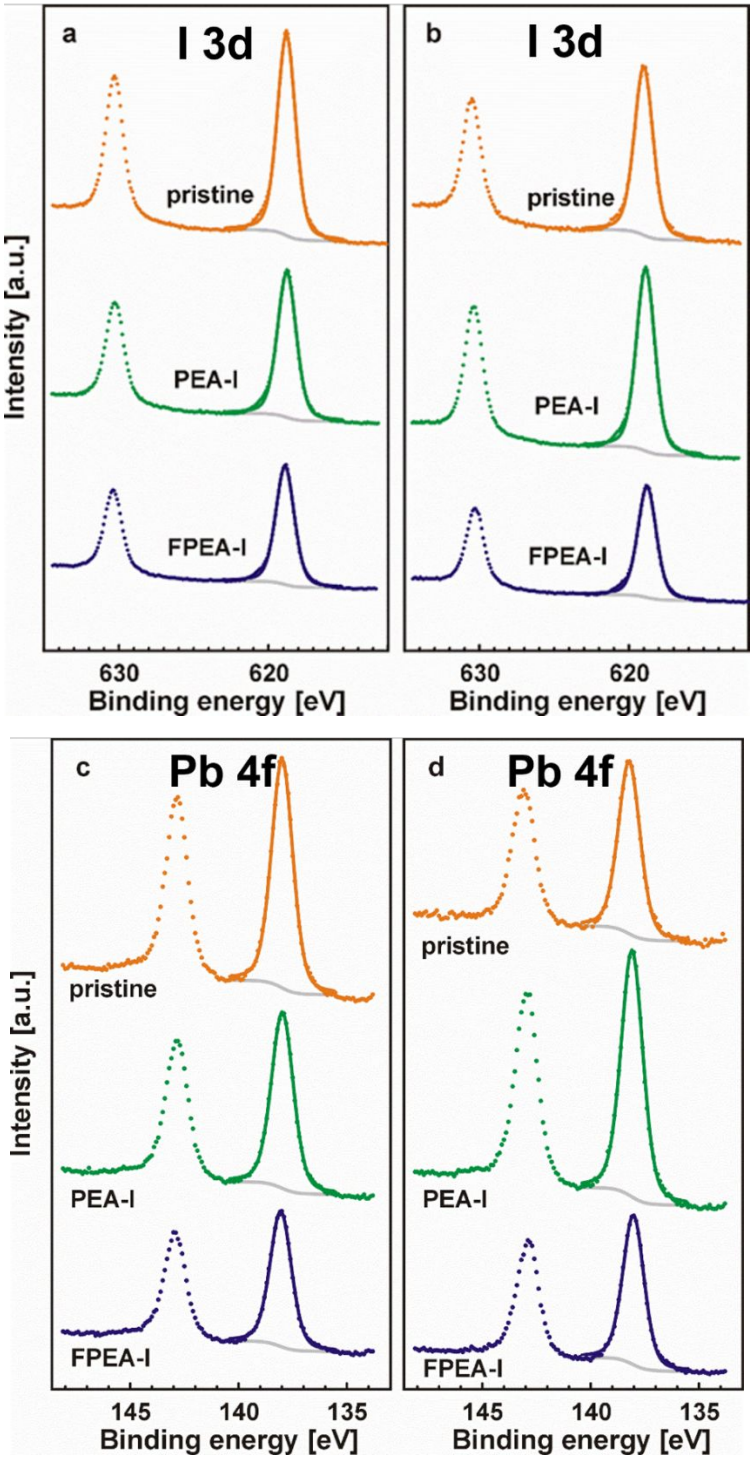

Figure S16. XPS spectra of the iodine (I 3d) and lead (Pb 4f) core level, measured for the three sample types, taken (a, c) before light soaking test, and (b, d) after 1000 hours of light illumination.

References:

(1) Yang, X.; Luo, D.; Xiang, Y.; Zhao, L.; Anaya, M.; Shen, Y.; Wu, J.; Yang, W.; Chiang, Y. H.; Tu, Y.; Su, R.; Hu, Q.; Yu, H.; Shao, G.; Huang, W.; Russell, T. P.; Gong, Q.; Stranks, S. D.; Zhang, W.; Zhu, R. Buried Interfaces in Halide Perovskite Photovoltaics. *Adv. Mater.* **2021**, *33* (7), 1–10. https://doi.org/10.1002/adma.202006435.

(2) Perdew, J. P.; Burke, K.; Ernzerhof, M. Generalized Gradient Approximation Made Simple. *Phys. Rev. Lett.* **1996**, *77* (18), 3865–3868. https://doi.org/10.1103/PhysRevLett.77.3865.

(3) Grimme, S.; Antony, J.; Ehrlich, S.; Krieg, H. A Consistent and Accurate Ab Initio Parametrization of Density Functional Dispersion Correction (DFT-D) for the 94 Elements H-Pu. *J. Chem. Phys.* **2010**, *132* (15). https://doi.org/10.1063/1.3382344.

(4) Giannozzi, P.; Baroni, S.; Bonini, N.; Calandra, M.; Car, R.; Cavazzoni, C.; Ceresoli, D.; Chiarotti, G. L.; Cococcioni, M.; Dabo, I.; Dal Corso, A.; De Gironcoli, S.; Fabris, S.; Fratesi, G.; Gebauer, R.; Gerstmann, U.; Gougoussis, C.; Kokalj, A.; Lazzeri, M.; Martin-Samos, L.; Marzari, N.; Mauri, F.; Mazzarello, R.; Paolini, S.; Pasquarello, A.; Paulatto, L.; Sbraccia, C.; Scandolo, S.; Sclauzero, G.; Seitsonen, A. P.; Smogunov, A.; Umari, P.; Wentzcovitch, R. M. QUANTUM ESPRESSO: A Modular and Open-Source Software Project for Quantum Simulations of Materials. *J. Phys. Condens. Matter* **2009**, *21* (39). https://doi.org/10.1088/0953-8984/21/39/395502.

(5) Stoumpos, C. C.; Malliakas, C. D.; Kanatzidis, M. G. Semiconducting Tin and Lead Iodide Perovskites with Organic Cations: Phase Transitions, High Mobilities, and near-Infrared Photoluminescent Properties. *Inorg. Chem.* **2013**, *52* (15), 9019–9038. https://doi.org/10.1021/ic401215x.

(6) MacRae, C. F.; Sovago, I.; Cottrell, S. J.; Galek, P. T. A.; McCabe, P.; Pidcock, E.; Platings, M.; Shields, G. P.; Stevens, J. S.; Towler, M.; Wood, P. A. Mercury 4.0: From Visualization to Analysis, Design and Prediction. *J. Appl. Crystallogr.* **2020**, *53*, 226–235. https://doi.org/10.1107/S1600576719014092.

(7) Zhao, Y.; Zhang, J. Microstrain and Grain-Size Analysis from Diffraction Peak Width and Graphical Derivation of High-Pressure Thermomechanics. *J. Appl. Crystallogr.* **2008**, *41* (6), 1095–1108. https://doi.org/10.1107/S0021889808031762.

(8) Dasgupta, S.; Misztal, K.; Fuentes Pineda, R.; Mróz, W.; Pawlaczyk, Ł.; Serafińczuk, J.; Barker, A. J.; Ahmad, T.; Herman, A. P.; Sahayaraj, S.; Kudrawiec, R.; Petrozza, A.; Dudkowiak, A.; Wojciechowski, K. New Synthetic Route of Ultrapure Alkylammonium Iodides for Perovskite Thin Films of Superior Optoelectronic Properties. *Energy Technol.* **2020**, *8* (10), 1–12. https://doi.org/10.1002/ente.202000478.

(9) Moszak, K.; Olszewski, W.; Pucicki, D.; Serafińczuk, J.; Opołczyńska, K.; Rudziński, M.; Kudrawiec, R.; Hommel, D. Verification of Threading Dislocations Density Estimation Methods Suitable for Efficient Structural Characterization of AlxGa1-XN/GaN Heterostructures Grown by MOVPE. *J. Appl. Phys.* **2019**, *126* (16). https://doi.org/10.1063/1.5100140.

(10) Yang, J.; Cao, Q.; He, Z.; Pu, X.; Li, T.; Gao, B.; Li, X. The Poly(Styrene-Co-Acrylonitrile) Polymer Assisted Preparation of High-Performance Inverted Perovskite Solar Cells with Efficiency Exceeding 22%. *Nano Energy* **2021**, *82* (December 2020), 105731. https://doi.org/10.1016/j.nanoen.2020.105731.

(11) Muneeswaran, M.; Jegatheesan, P.; Gopiraman, M.; Kim, I. S.; Giridharan, N. V. Structural, Optical, and Multiferroic Properties of Single Phased BiFeO3. *Appl. Phys. A Mater. Sci. Process.* **2014**, *114* (3), 853–859. https://doi.org/10.1007/s00339-013-7712-5.

(12) Bi, D.; Tress, W.; Dar, M. I.; Gao, P.; Luo, J.; Renevier, C.; Schenk, K.; Abate, A.; Giordano, F.; Correa Baena, J. P.; Decoppet, J. D.; Zakeeruddin, S. M.; Nazeeruddin, M. K.; Grätzel, M.; Hagfeldt, A. Efficient Luminescent Solar Cells Based on Tailored Mixed-Cation Perovskites. *Sci. Adv.* **2016**, *2* (1). https://doi.org/10.1126/sciadv.1501170.

(13) Wetzelaer, G. A. H.; Kuik, M.; Lenes, M.; Blom, P. W. M. Origin of the Dark-Current Ideality Factor in Polymer:Fullerene Bulk Heterojunction Solar Cells. *Appl. Phys. Lett.* **2011**, *99* (15). https://doi.org/10.1063/1.3651752.

(14) Caprioglio, P.; Stolterfoht, M.; Wolff, C. M.; Unold, T.; Rech, B.; Albrecht, S.; Neher, D. On the Relation between the Open-Circuit Voltage and Quasi-Fermi Level Splitting in Efficient Perovskite Solar Cells. *Adv. Energy Mater.* **2019**, *9* (33). https://doi.org/10.1002/aenm.201901631.

(15) Kim, S.; Jang, J. H.; Wu, Z.; Lee, M. J.; Woo, H. Y.; Hwang, I. Interfacial Defects Change the Correlation between Photoluminescence, Ideality Factor, and Open-Circuit Voltage in Perovskite Solar Cells. *Small* **2021**, *17* (33), 1–10. https://doi.org/10.1002/smll.202101839.